Ultrahigh Oxygen Evolution Reaction Activity Achieved Using Ir Single Atoms on Amorphous CoO_X Nanosheets

Chao Cai[a,b], Maoyu Wang[c], Shaobo Han[a,b], Qi Wang,[b] Qing Zhang,[b] Yuanmin Zhu,[b] Xuming Yang,[b] Duojie Wu,[b] Xiaotao Zu[a*], George E. Sterbinsky,[d] Zhenxing Feng[c*], Meng Gu[b*]

[a] School of Physics, University of Electronic Science and Technology of China, Chengdu 610054, China.

[b] Department of Materials Science and Engineering, Guangdong Provincial Key Laboratory of Energy Materials for Electric Power，Southern University of Science and Technology, No. 1088 Xueyuan Blvd, Shenzhen, Guangdong 518055, China

[c] School of Chemical, Biological, and Environmental Engineering, Oregon State University, Corvallis, OR 97331, USA

[d] Advanced Photon Source Argonne National Laboratory, Argonne, IL 60431, USA

* Email: xtzu@uestc.edu.cn; gum@sustech.edu.cn; zhenxing.feng@oregonstate.edu

KEYWORDS

Iridium oxides, cobalt oxides, amorphous nano sheets, single atom catalysts, hierarchical microstructures.

ABSTRACT

Developing efficient electrocatalysts for oxygen evolution reaction (OER) is important for renewable energy storage. Here we design high-density Ir single-atom catalysts supported by CoO_x amorphous nanosheets (ANSs) for OER. Experimental results show that Ir single-atoms are anchored by abundant surface-absorbed O in CoO_x ANSs. The Ir single-atom catalysts possess ultrahigh mass activity that is 160-fold of commercial IrO_2. The OER of $IrCoO_x$ ANSs reached a record-low onset overpotential of less than 30 mV. The in-situ X-ray absorption spectroscopy reveals that the Ir-O-Co pairs directly boosted the OER efficiency and enhanced the Ir stability.

Industrial chemical reactions utilize catalysts to increase the production rate of a desired product and reduce the energy costs.[1-2] Therefore, developing efficient catalysts can reduce energy costs and selectively promote the production of value-added chemicals.[3] The sluggish kinetics of the oxygen evolution reaction (OER) seriously limit the practical applications of hydrogen production[4-6] and carbon dioxide reduction in aqueous media.[7-10] To date, Ru/Ir –based metals and their oxides are well known as the most efficient OER catalysts.[11] However, their scarcity and high price are major barriers for their application.[12-13] Therefore, exploring highly efficient catalysts with reduced Ru/Ir usage is necessary for practical applications. Many attempts have been made, such as alloying with transition metals, core-shell approaches, and single atom catalysts (SACs), etc.[4, 14-16]

The high free energy of single atoms in SACs ensures an easier adsorption process than traditional nano-catalysts, further boosting their catalytic activity.[17] Adsorption of molecules on surfaces often leads to varied coordination environments of SACs during pre-activation or initial reaction processes.[18] The synergistic Ru sites in the Ru-FeCo$(OH)_x$ SACs are the active reaction sites, which significantly promote the OER activity.[19] Unfortunately, once the highly active SACs are put in liquid, the active atoms often suffer from surface etching, subsequently leading to activity loss.[20] In addition, the harsh reaction may trigger the aggregation of SACs, which weakens the synergistic effect between single atoms and the matrix and lowers the adsorption-desorption efficiency as well as catalytic activity/stability.[17, 21-22] Moreover, harsh catalytic reaction leads to the structural transformation and breakdown of catalysts.[23-24] Currently, these issues of SACs still delay their various practical applications.

In this work, we synthesized CoO_x ANSs doped with Ir single atoms. The $IrCoO_x$ ANSs possess a thickness of *ca.* 1 nm and ultrahigh surface areas of 213 m^2/g. By tuning the stoichiometric ratio of Ir/Co, we achieve the highest mass OER activity reported to date. We used a combination of aberration corrected scanning transmission electron microscopy (STEM) and *in-situ* X-ray absorption spectroscopy (XAS) to understand the catalyst structure and related reaction mechanisms.

RESULTS and DISCUSSIONS

As $Ir_1Co_{13.3}O_{20.1}$-(Sample 4) ANSs with an Ir/Co ratio of ~7:93 shows the best activity among all $IrCoO_x$ ANSs (Figure S1), we focus on the structural characterization of $Ir_1Co_{13.3}O_{20.1}$. The relative Ir/Co ratio determined by inductively coupled plasma optical emission spectroscopy (ICP-OES) is shown in Table S1. Scanning electron microscopy (SEM), transmission electron

microscopy (TEM), double Cs-corrected STEM, powder X-ray diffraction (XRD), and N_2 adsorption-desorption tests are employed to clarify the morphology and structure of as-prepared $Ir_1Co_{13.3}O_{20.1}$ ANSs. The $Ir_1Co_{13.3}O_{20.1}$ possess a hierarchical microstructure composed of curly nanosheets (Figure 1a). The selected area electron diffraction (SAED) in the inset of Figure 1b reveals the amorphous nature of the as-prepared $Ir_1Co_{13.3}O_{20.1}$. The amorphous feature of $Ir_1Co_{13.3}O_{20.1}$is also verified by XRD (Figure S2). Benefitting from the ultrathin feature of CoO_x ANSs (thickness of ca. 1 nm, as shown in Figure 1c), the $Ir_1Co_{13.3}O_{20.1}$ possess large surface area determined to be *ca.* 213.3 m^2/g (Figure S3). This is larger than many reported metal oxides and carbon-based materials, which typically have surface areas smaller than 180 m^2/g.[25-27] The formation of an ultrathin layered structure can be attributed to the hexadecyltrimethylammonium bromide (CTAB, 0.05 M) and the fast precipitation caused by $NaBH_4$. The concentration of CTAB is *ca.* 2.5-fold of its second critical micelle concentration (0.02 M), leading to the formation of a CTAB bilayer structure in solution.[28] The $NaBH_4$ leads the fast formation of CoB_x that can be easily oxidized by O and H_2O. Therefore the newborn CoB_x in the system tends to form CoO_x amorphous layers.[29] Without CTAB use in reaction solution, the precipitation can be CoB_x amorphous particles.[30]

The catalytic activity is impacted by the distribution and structure of Ir atoms. Thus we used STEM to clarify the nanostructure of $Ir_1Co_{13.3}O_{20.1}$. The low magnification STEM image finds no Ir particles in $Ir_1Co_{13.3}O_{20.1}$ (Figure 1d). The energy dispersive spectrum (EDS) at low magnification demonstrates a homogeneous distribution of Ir, Co and O (Figure 1e). The high magnification STEM image demonstrates the monodispersed Ir single atoms (brighten spots marked by red circles in Figure 1f) on CoO_x ANSs. Unlike multi-step preparation of Au single atoms on $FeNi(OH)_x$ nanosheets[13] and Pt single atoms on CeO_2,[17] $Ir_1Co_{13.3}O_{20.1}$ ANSs are prepared

in one pot. Due to the large surface area and high chemical activity, two-dimensional CoO_x ANSs may adsorb many oxygen atoms on the surface. Surface-absorbed oxygen and surfactant could be the major contributors to the formation of Ir single atoms. The anchoring of Ir atoms can occur at the sites with surface-absorbed oxygen, because the strong bonding of O firmly captures the Ir atoms. The surfactant can avoid the regrowth of Ir. Using this idea, we successfully synthesized $IrNiO_x$ ANSs using an approach similar to $IrCoO_x$ ANSs (Figure S4). This result demonstrates that reduction of noble metal on ANSs with abundant surface-absorbed oxygen could be a reliable approach to synthesize various SACs.

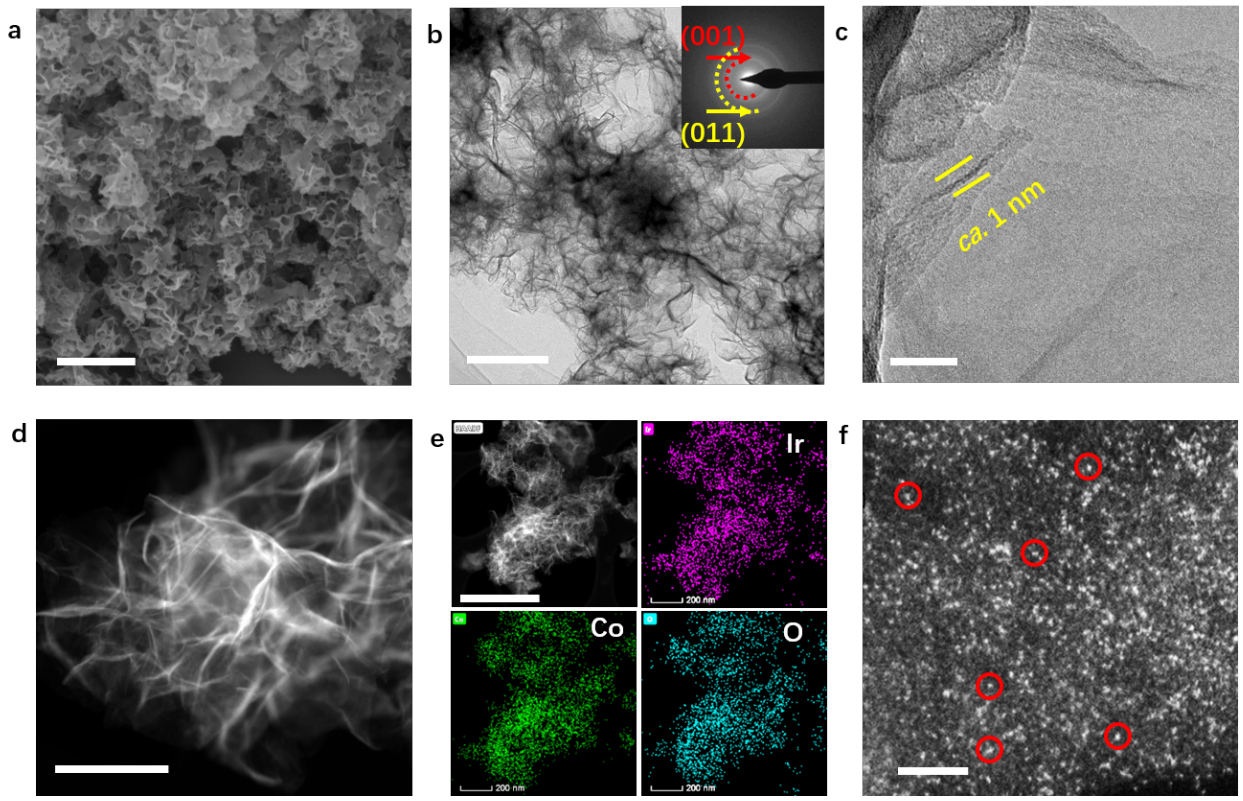

Figure 1. Structural characterization of $Ir_1Co_{13.3}O_{20.1}$. SEM image (a), low magnification TEM image (b), high magnification TEM image (c), HAADF image (d), EDS mapping (e), and high

magnification HAADF image (f) of $Ir_1Co_{13.3}O_{20.1}$. Ir single atoms anchor on CoO_x ANSs and are well dispersed. The brighten spots in Figure 1f correspond to Ir atoms, exemplified by red circles marked. Scale bar in a-f is 1 um, 200 nm, 20 nm, 100 nm, 500 nm, and 1 nm, respectively.

We used Ir/Co-based materials as catalysts for OER in 1 M KOH using a three-electrode system. Relative data is shown in Figure 2, where all the current densities are normalized by the geometric area of the glass carbon electrode (GCE). The $Ir_1Co_{13.3}O_{20.1}$ possess the highest OER activity among all reported OER catalysts to date (Table S2). As shown in Figure 2a, $Ir_1Co_{13.3}O_{20.1}$ exhibit much better OER activity than CoO_x ANSs and IrO_2 over the entire potential range. Figure 2b shows that $Ir_1Co_{13.3}O_{20.1}$ require a low overpotential of only 152±5.2 mV to achieve 10 mA/cm^2, much lower than pure CoO_x ANSs (330.1±12.5 mV) and commercial IrO_2 (320.0±10.1 mV). The $Ir_1Co_{13.3}O_{20.1}$ have the lowest Tafel slope (*ca.* 60.5±2.8 mV/dec) among these prepared catalysts, and it is even lower than commercial IrO_2 (*ca.* 65.6±2.7 mV/dec) as shown in Figure 2c. At 1.485 V *v.s.* RHE, the $Ir_1Co_{13.3}O_{20.1}$ possess specific current density of 160 mA/cm^2 (mass activity of 1412 A/g), which is 160-fold of commercial IrO_2 (1 mA/cm^2). To clarify the origin of such superior OER activity, we employed double layer capacitance (C_{dl}) test to calculate the electrochemical surface area (ECSA) (Figure 2e), which is sensitive to the exposed atoms in OER. The $Ir_1Co_{13.3}O_{20.1}$ possess *ca.* 2-fold ECSA value compared to CoO_x ANSs, while surprisingly the catalytic activity of $Ir_1Co_{13.3}O_{20.1}$ is *ca.* 40-fold of CoO_x ANSs (Figure 2d). These results show that its high OER activity is due to not only increasing ECSA, but also the high intrinsic activity of Ir for OER. The high intrinsic catalytic activity of Ir is further promoted by the support of ultrathin amorphous CoO_x ANSs (Figure S5). The commercial IrO_2 sample is also characterized using STEM, XRD, and XPS (Figure S6 to S8) to get further insights regarding to its physical structure, morphology, and surface chemistry information. By carefully comparing the polarization curve

that normalized by surface area and ECSA (Figure S8a&b), we found that the $Ir_1Co_{13.3}O_{20.1}$ possess higher intrinsic activity than IrO_2. The aggregated Ir nanoparticles on CoO_x NSs shows better OER activity than pure CoO_x NSs, but worse than $Ir_1Co_{13.3}O_{20.1}$ (Figure S8c&d), confirming that the OER activity in Ir/Co NSs is critically affected by the Ir local coordination environments and morphology. In addition, as shown in Figure 2f, electrochemical impedance spectrum (EIS) results testify that the charge transport resistance (R_{ct}) of $Ir_1Co_{13.3}O_{20.1}$ is 11.8±0.9 Ω, which is around 1/5 of CoO_x ANSs (56.4±2.3 Ω). Therefore, such superior OER activity of $Ir_1Co_{13.3}O_{20.1}$ can be ascribed to the largely enhanced chemical active areas, high intrinsic activity of Ir on CoO_x ANSs, and super-fast charge transport from catalysts to support.

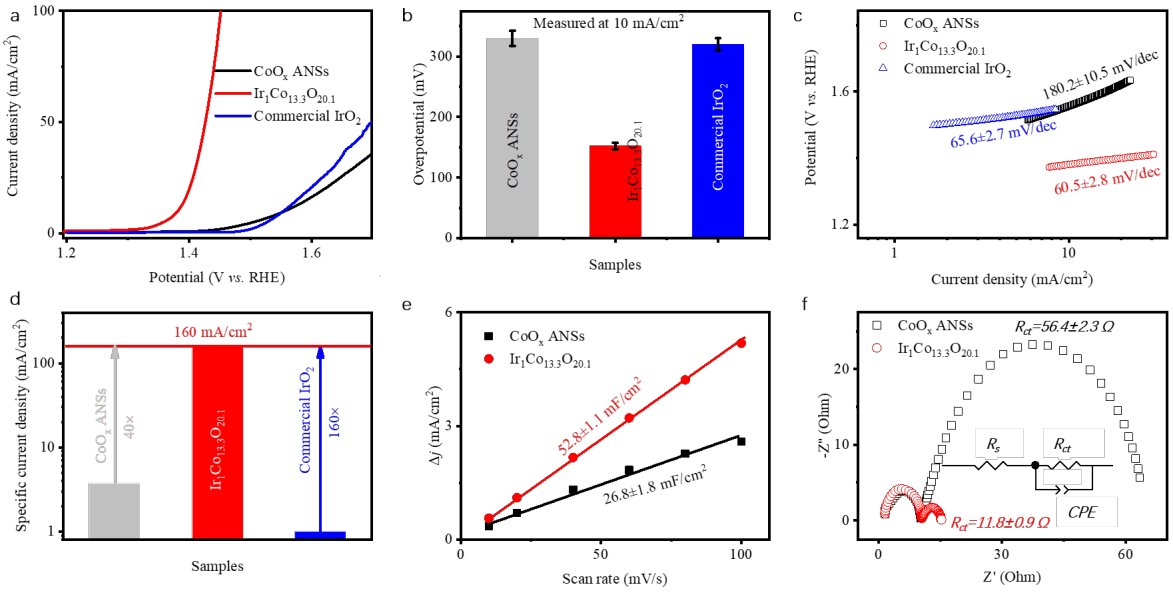

Figure 2. Electrochemical characterizations of different catalysts. Polarization curves (a), collection of overpotential at 10 mA/cm^2 (b), Tafel plots (c), specific current density at 1.485 V *v.s.* RHE (d)， C_{dl} values (e), and Nyquist plots (f) of CoO_x ANSs and $Ir_1Co_{13.3}O_{20.1}$ ANSs. The inset in Figure 2f is the equivalent circuits for R_{ct} calculation. The $Ir_1Co_{13.3}O_{20.1}$ANSs show far better OER performance than CoO_x ANSs and IrO_2.

The abundant surface-absorbed oxygen and strong synergistic effect between Ir and Co also play critical roles in promoting OER activity. X-ray photoelectron spectroscopy (XPS) was used to clarify the valence of metal cations and oxygen states in $Ir_1Co_{13.3}O_{20.1}$ and CoO_x ANSs (Figure 3). Figure 3a shows the survey spectrum of $Ir_1Co_{13.3}O_{20.1}$ and CoO_x ANSs. Figure 3b collects the fitted Co 2p fine spectrum. The fitted peaks of Co $2p_{3/2}$ correspond to Co^{3+} (*ca.* 780.2 eV) and Co^{2+} (*ca.* 782.1 eV), respectively.[25, 27] The increased Co^{3+}/Co^{2+} ratio after Ir loading indicates also a higher content of oxygen, forming possible Ir-O-Co pairs. Figure 3c shows the normalized O 1s spectrum. The O 1s spectra extends at high energy edge in $Ir_1Co_{13.3}O_{20.1}$. The adsorption O content is increased after Ir loading (Figure S9a), which can increase average valence of catalysts, and thus enhance the OER activity.[31] To further clarify the oxidation state of Co and O, the electron energy loss spectroscopy (EELS) is carried out to determine the average valance of Co and O/Co content ratio as shown in Figure 3d. The valence states of Co can be measured according to the L_3/L_2 white-line intensity ratios. In our work, the integrated L_3/L_2 ratio of $Ir_1Co_{13.3}O_{20.1}$ is calculated to be 2.78 which is lower than 3.13 of CoO_x ANSs, verifying the higher Co valence. Correspondingly, the O *K* edge fine structure also shows a higher pre-peak intensity after Ir-loading on the CoO_x sample, which correspondingly indicates a higher Co oxidation state. The integrated area ratio of O *K*-edge to Co *L*-edge in $Ir_1Co_{13.3}O_{20.1}$ is calculated to be 0.38, which is larger than that of CoO_x ANSs (0.27), confirming a higher O content in $Ir_1Co_{13.3}O_{20.1}$. In this case, the Ir loading can promote the O adsorption efficiency in $Ir_1Co_{13.3}O_{20.1}$ and increase the oxidation states of cobalt. The XPS peaks of Ir corresponds to various valance states as shown in Ir 4f spectra (Figure S7c). The existence of Ir^{3+}/Ir^{4+} cations demonstrates a strong bonding between Ir and oxygen atoms including the ones absorbed on the surface. These results show that controlling the amount of surface-absorbed

oxygen atoms can be fine-tuned by changing Ir loading. In the same time, Ir loading modulates the Co valence of the matrix.

To get further insight into the Ir-Co coupling effect, *in-situ* XAS was carried out to identify the oxidization state and local coordination environment of Ir and Co. Co K-edge X-ray absorption near edge structure (XANES) shows that Co cations in CoO_x ANSs have a slightly higher oxidation state than crystalline CoO (Figure 3e and S10), which is caused by abundant surface-absorbed oxygen environments in CoO_x ANSs. The surface-absorbed oxygen can firmly capture Ir atoms by forming Ir-O-Co bonding that is confirmed by extended X-ray absorption fine structure (EXAFS) fitting. Interestingly, Co is further oxidized after loading Ir on the surface. With surface-absorbed oxygen increasing, the higher electron affinity of Ir (150 kJ/mol) than Co (64 kJ/mol) leads to re-centering of the 3d electrons of Co towards Ir via Ir-O-Co bonding. To probe the exact local structure, the EXAFS measurements are performed (shown in Figure 3f) and the model-based analysis (Figure S9 and Table S4) confirms that CoO_x ANSs have surface-absorbed oxygen due to less Co-Co scattering paths which are related to Co-O-Co bond in the CoO model (also seen at $2Å < R < 3$ Å region in Figure 3f) comparing with crystalline CoO.

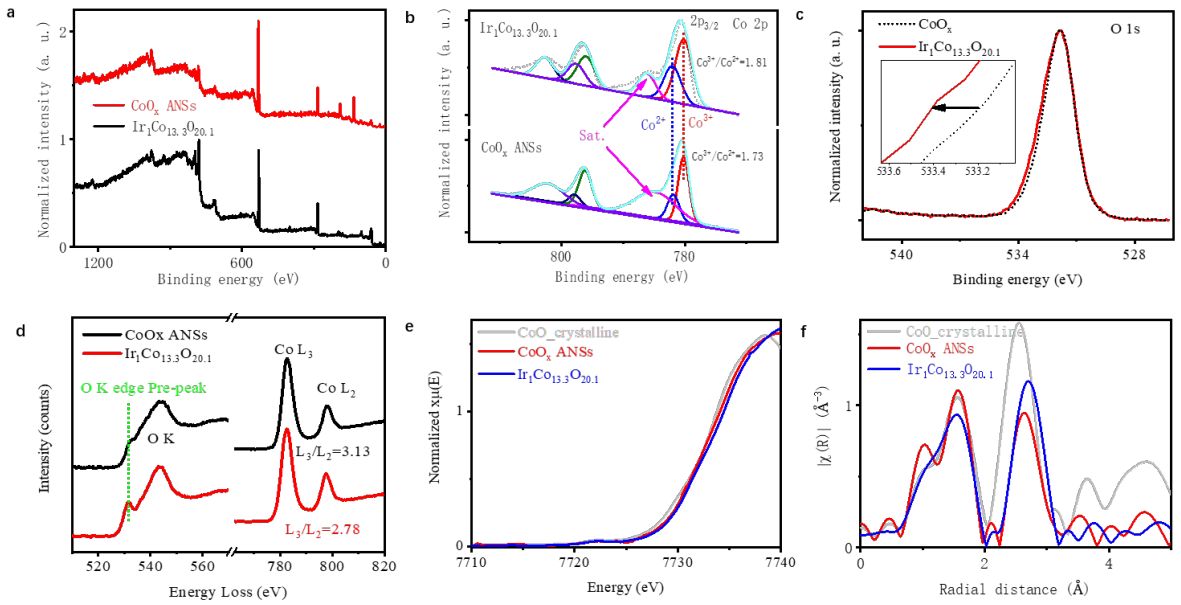

Figure 3. Surface chemistry and structures of $Ir_1Co_{13.3}O_{20.1}$ and CoO_x ANSs. XPS results of $Ir_1Co_{13.3}O_{20.1}$ and CoO_x ANSs (a to d). Survey spectrum (a), Co 2p spectrum (b), O 1s spectrum (c), and EELS spectrum of O K- and Co L-edge (d). Co K-edge (e) XANES and (f) EXAFS of $Ir_1Co_{13.3}O_{20.1}$ and CoO_x ANSs.

The catalytic activity of Ir-based catalysts usually being affected by the surrounded coordination environment change and their valence variation during OER. In our experiments, the OER performance improvement can be attributed to the change in the OH^- free energy, the O^{2-} to OH^- adsorption Gibbs energy difference, and the different electron affinity between Ir and Co.[32-33] The much higher electron affinity of Ir can attract the highly concentrated electrons moving toward Ir sites, which leads to the preferential adsorption of OH^- and intermediates during OER, thus promoting the formation of high valence Ir cations during OER. Herein, the amount of Ir doping also influences the OER activity by changing the number of active sites. Figure S1 shows that $Ir_1Co_{13.3}O_{20.1}$ have the highest OER activity compared to other samples. Therefore, optimized stoichiometry of $IrCoO_x$ ANSs could effectively promote active Ir-O-Co pairs formation, leading

to a much better OER performance. It is reported that surface-absorbed O can promote OER and be released by heat-treatment.[26, 34] In our experiment, the annealed $Ir_1Co_{13.3}O_{20.1}$ with surface-absorbed O released has much lower OER activity than $Ir_1Co_{13.3}O_{20.1}$ (Figure S10).

The catalysts with high activity usually possess structural instability, leading to deactivation of the catalysts.[16, 35-38] The current density of $Ir_1Co_{13.3}O_{20.1}$ is stable after 10 h, while that of IrO_2 decreases by 72 % (Figure S11a). The decreased OER activity of IrO_2 originates from the fast degradation of active Ir in alkaline solution by forming water soluble IrO_3^{2-}.[39-40] The $Ir_1Co_{13.3}O_{20.1}$ also show high stability under large current (Figure S11b). *Ex-situ* STEM is used to check the structure of $Ir_1Co_{13.3}O_{20.1}$ after OER (Figure S12). The remaining isolated Ir single atoms on CoO_x ANSs demonstrate the high structural stability in OER for 10 h. The highly structural stability of Ir single atoms may be responsible for the stable OER activity. However, the matrix (CoO_x) may dissolve during OER, which can lead to the Ir dissolution. Therefore, we examined the Ir ions residual in electrolyte after OER (Table S3). The low Ir dissolution rate indicates a high stability of Ir again. The $Ir_1Co_{13.3}O_{20.1}$ exhibits higher OER activity in 2M KOH than in 1M KOH, and exhibits a 3-fold increase at 60℃ in 1 M KOH (Figure S13). To understand how catalysts restructure in reactions, *in-situ* XAS was used.[41-43] In Figure 4a, at the open-circle voltage (OCV), the energy at which the white line of the Ir L-edge XANES lies is in between those of Ir and IrO_2, suggesting the co-existence of high valence Ir^{4+} cations and Ir^0 atoms in the pristine sample. When higher voltage is applied, the white line intensity increases and the peak shifts to higher energy (Figure 4a and S16), indicating the increase of the Ir oxidation state. Since high valance Ir is believed to be active for OER,[25, 27] the increase of the high valance Ir ratio promotes the OER reaction. When the applied potential returned to OCV, Ir was reduced back but didn't overlap with

the one at OCV.[44] This can be resulted by the further oxidation of Ir ions at high potential during OER.

Furthermore, the EXAFS fitting of $Ir_1Co_{13.3}O_{20.1}$ pristine material (Figure 4c) shows that Ir is bonded with 6 oxygen (Table S5). The Ir-Co scattering pathway in pristine is around 3.56 Å, much longer than the same Ir-Co scattering paths (2.92 Å) during the reaction (Table S6). This suggests a strong Ir and Co interaction after applying voltage, which subsequently causes more oxidized Co cations in reactions. All those results are consistent with XPS results. Note that Ir-Ir scattering cannot be added in our model to produce meaningful fitting results for both pristine and reacted materials in our EXAFS analysis, which further verifies that most Ir is likely singly distributed on the CoO_x ANS surface, consistent with the conclusions drawn from the STEM results shown in Figure 1.

The restructuring of Ir cations is responsible for the high OER activity (Figure S5). As shown in Figure 4b, the Ir local coordination environment varies a lot during the reaction. The Ir-O peak becomes shaper and bonding length becomes shorter during OER due to the increased Ir oxidization state, which is also a result of stronger Ir bonding with O to form IrO_x (x near to 6) in reaction. The EXAFS analysis of Ir-O shows that the average coordination numbers (CNs) and bond-length of Ir-O decrease during OER (Figure 4f, Figure S17 and Table S7). These result from the restructuring of $Ir_1Co_{13.3}O_{20.1}$ in reaction conditions. Once the potential is applied, the substrate-catalyst interaction becomes stronger, thus trapping and stabilizing the surface Ir atoms into CoO_x ANSs and forming a new peak around 2.5 Å which is corresponding to shorter Ir-Co scattering path or Ir-O-Co bonding (Figure 4b&e). This is similar to our previous work on single atom Ru anchored on cobalt-iron layerd double hydroxides, which has a shorter and stable Ru-O-M (M=Co or Fe) bond in OER compared to that in as-synthesized catalyst.[41] In our case, the Ir

cations in their first shell are not fully coordinated in OER. These under-coordinated Ir cations can adsorb OH^- efficiently. When the potential reaches 1.26 V, the surface-absorbed O and Ir-O start to be oxidized, leading to the decrease of Ir-O CNs. The Ir will capture the H_2O or OH^- from electrolyte to become fully coordinate after the voltage is back to OCV (Figure 4c&d; table S5). These results show that the OER start at an onset potential of <30 mV. In contrast, the average CN of Ir-O-Co bond (the second shell) is substantially increased, suggesting that O between Ir and Co are mostly oxidized during OER. These Ir-O-Co remains visible after OER stop (Figure 4b), as Ir/Co can get O from alkaline solution. In this case, the active Ir-O-Co can be strongly anchored on CoO_x ANSs during OER, and thus ensuring high stability in alkaline solution. In short, such high OER activity of $Ir_1Co_{13.3}O_{20.1}$ is associated with those pre-adsorpted O and the O in Ir-O-Co. In addition, the replenished O species bonding with Ir continually get preferentially oxidized in OER reaction.

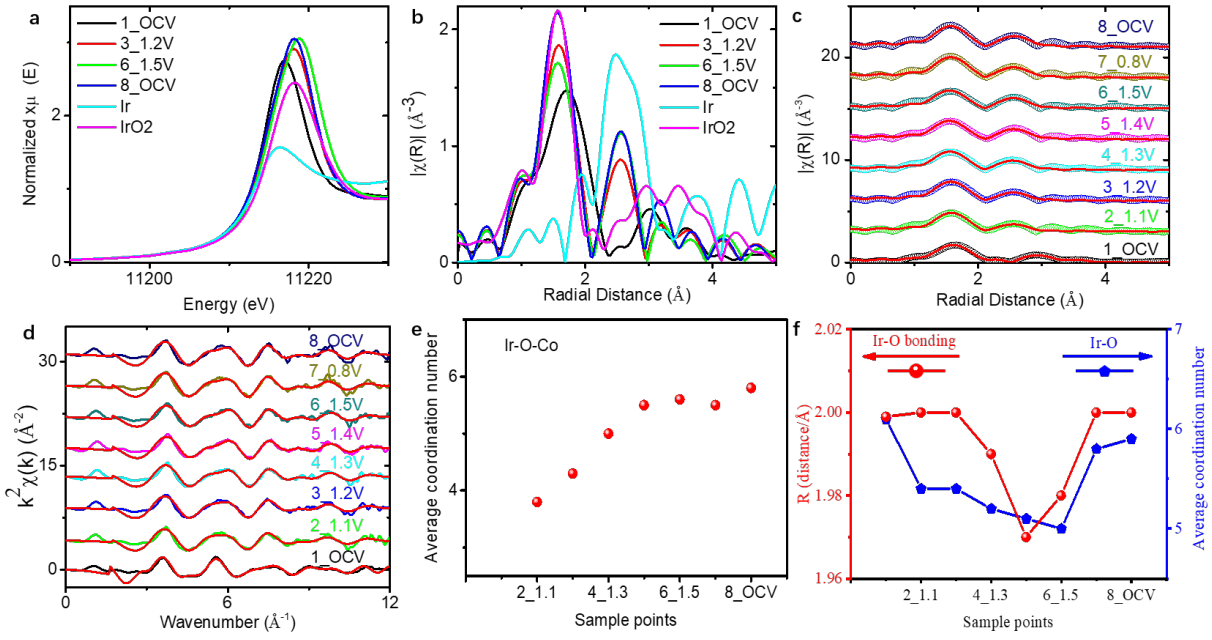

Figure 4. XAS results of $Ir_1Co_{13.3}O_{20.1}$. *In-situ* Ir L-edge (a) XANES and (b) EXAFS under various reaction potential; Fourier Transfer EXAFS fitting of in-situ Ir during the reaction (c) R-space and (d) k-space. The average coordination number of Ir-O-Co during OER (e). The Ir-O bonding distance and average coordination number of Ir-O during OER (f).

CONCLUSIONS

In summary, we demonstrated that the Ir/Co synergistic effect can be effectively manipulated by controlling the O state in SACs. The $Ir_1Co_{13.3}O_{20.1}$ANSs start the OER at low onset potential of <30mV. This material shows superior OER activity which is 160-fold of commercial IrO_2. The Ir single atoms on CoO_x ANSs enable the ultrahigh utilization of Ir, leading to the lowest cost for industrial applications. The in-situ XANES results disclose that the O in the *in-situ* formed Ir-O-Co get preferentially oxidized with smaller overpotential, magnifying OER activity. We believe that our findings could be a giant leap towards designing highly active catalysts for various applications, such as metal-air batteries and hydrogen production from water electrolysis.

EXPERMENTAL

Chemicals

All the chemicals are directly used in experiments without further purification. $Co(NO)_3 \cdot 6H_2O$ (>98 %), $Ni(NO)_3 \cdot 6H_2O$ (>98 %), cetyltrimethylammonium bromide (CTAB, >95 %), $H_2IrCl_6 \cdot 6H_2O$ (> 40 %, metal basis), sodium borohydride (SB, >99 %), isopropanol (>95 %), acetone (>95 %), and NaOH (>99.999 %) were purchased from Aldrich. Nafion solution was purchased from sigma (5 wt. % aqueous solution). Commercial IrO_2 is purchased from Macklin Biochemical (99.9 % metal basis, Ir>84.5 %). Nickel Foam was purchased from Shenzhen Green and Creative Environmental Science and Technology Co. Ltd.

Synthesis of Sample N series of $IrCoO_x$ ANSs

This experiment is carried out at room temperature in air. 4 mmol $Co(NO)_3 \cdot 6H_2O$ is added into 100 mL water (contains 50 mmol CTAB) with magnetic stirring to form solution A. After 20 min, 6 mmol SB is added into solution A quickly. After reacting for 30 min, amount of $H_2IrCl_6 \cdot 6H_2O$ aqueous solution (N=0.5 ml, 1 ml, 2 ml, 3 ml, and 4 ml) (40 mg/mL) is added. The system is held for another 1 h with magnetic stirring. Then 1 mmol SB is added into system and held for 20 min. The precipitation is washed by water and acetone for 5 times. Those black powders are dried in vacuum oven at 80 ℃ for whole night. The precipitation is collected as $IrCoO_x$-(Sample N with N=0.5, 1, 2, 3, 4) ANSs. The yield of $IrCoO_x$-(Sample 4) is ca. 648 mg. The mass loading of Ir in $IrCoO_x$-(Sample 4) is ca. 20 wt. %.

Synthesis of Ir nanoparticles/CoO_x

4 mL $H_2IrCl_6 \cdot 6H_2O$ aqueous solution and 4 mmol $Co(NO)_3 \cdot 6H_2O$ are added into 100 mL water (contains 50 mmol CTAB) with magnetic stirring to form transparent solution. Then, 6 mmol SB is added into solution quickly. After reacting for 30 min, the precipitation is washed, dried, and collected as Ir nanoparticle on CoO_x.

Annealing of $Ir_1Co_{13.3}O_{20.1}$

20 mg prepared powders of $Ir_1Co_{13.3}O_{20.1}$ (4 ml $H_2IrCl_6 \cdot 6H_2O$ aqueous solution is used during synthesizing process) are heated to 450 ℃ with a heat rating of 5 ℃/min and held for 2 h in air. After cooling down to room-temperature, the black powders are collected for following electrochemical characterization.

Synthesis of $IrNiO_x$ ANSs

$IrNiO_x$ ANSs are prepared similar to $Ir_1Co_{13.3}O_{20.1}$ ANSs, using $Ni(NO)_3 \cdot 6H_2O$ instead of $Co(NO)_3 \cdot 6H_2O$.

Synthesis of CoO_x ANSs

The CoO_x ANSs are prepared in a way similar to $IrCoO_x$-(sample N with N=0.5, 1, 2, 3, 4) ANSs synthesis without Ir using. The yield of CoO_x ANSs is 540 mg (the feeding amount is 4 mmol).

Structural characterization: The morphology and microstructure characterizations of the as-prepared samples were investigated by scanning electron microscopy (SEM) (FEI, Helios Nanolab 600i, 2kV), Transmission electron microscopy (TEM) and selected area electron diffraction (SAED) (FEI, ETEM, G2, 200kV), scanning transmission electron microscopy with an energy dispersive X-ray spectroscopy attachment (STEM-EDS, FEI Titan Themis, 300 kV). X-ray diffraction (XRD) (Bruker ECO D8 power X-ray diffractometer with Cu Kα radiation) were utilized to determine the crystal structure of the samples. The 20 mg powders ($IrCoO_x$-(Sample N with N=0.5, 1, 2, 3, 4) ANSs) is dissolved into 10 mL nitric acid (1 M), and then the mixed solution is sonicated for 3 min. This solution is heated to 180 ℃ for 4 h, and then the pink solution is collected for ICP-OES testing.

Electrochemical characterization: All experiments are carried out using CHI760e in a three-electrode system in a PTFE bottle. Rotate glassy disk carbon electrode (GCE) (3 mm) is the support of active materials to be used as working electrode. Ag/AgCl (saturated with 4 M KCl) and graphite rod are used as counter electrode and reference electrode, respectively. Electrolyte is 1 M KOH saturated with O_2 (99.999) %. Working electrode for Co-based NSs is prepared by drop 20 uL dispersion (catalyst ink (4 mg/mL) with water containing 10 uL 5 wt. % Nafion solution) on a GCE (polished by Al_2O_3). Cycling voltammetry (CV), linear sweep voltammetry (LSV) and

chronoamperometry are measured at 298 K, air and 10 mV/s (scan rate) on CHI 760e. After 10 h, the catalyst is washed by water and ethanol before characterized by STEM. The large current density test is carried out on a Nickel Foam (1 cm×0.5 cm). The catalyst loading on Nickel Foam is ca. 2.2 mg/cm^2. The prepared working electrode is soaked in 1 M KOH solution for 2 h to form a Na^+ Nafion before electrochemistry being conducted. 100 mL KOH solution is used for OER test.

EELS analysis: The L_3/L_2 edge ratio is performed through the second derivative method. We take the second derivative of the EELS of different samples and integrate the positive intensity of the specific edge window to extract the L_3/L_2 ratio. The O *K* edge/Co *L* edge ratio is also calculated using the same second derivative method.

In-situ and operando XAS measurement: In-situ XANES and EXAFS experiments were performed at the Advanced Photon Source (APS) beamline 9-BM-B&C of Argonne National Laboratory (ANL). The working electrodes were prepared by depositing 2mg catalyst on a 100 μm thick and 2.5 x 1.5 cm^2 carbon cloth to form a 0.5 x 1 cm^2 active area (catalysts loading is ca. 2.2 mg/cm^2). The working electrodes, counter electrodes (Pt) and reference electrodes (Ag/AgCl) were mounted onto a custom-designed *in-situ* XAS fluorescence cell.[43, 45] Electrochemical measurements were done by a Gamry 600 electrochemical workstation under oxygen gas flow. A Vortex ME4 detector was used to collect the Ir L-edge fluorescence signal while a Si(111) monochromator scanned the incident X-ray photon energy through the Ir L absorption edge. The Si (333) harmonic was rejected by a Rh coated focusing mirror with an incident angle of 2.8 mrad. Each selected potential (iR compensated) was held until sufficient data statistics of XAS were achieved. The X-ray beam was calibrated using a Ir metal pellet. Data reduction, data analysis, and EXAFS fitting were performed with the Athena, Artemis, and IFEFFIT software packages. Standard procedures were used to

extract the EXAFS data from the measured absorption spectra. The pre-edge absorption was fit with a line which was then subtracted from the full spectrum. The data was then normalized by dividing by a constant factor such that the post edge absorption has a value roughly equal to one. The post-edge background was determined using a cubic-spline-fit procedure and then subtracted to obtain the EXAFS.[43, 45] For model-based EXAFS analysis, all the scattering paths were generated by the FEFF calculation function in Artemis based on the crystal structure of IrCoO (Figure S18). Phase shifts and back-scattering amplitudes were generated by the FEFF calculations based on crystal structures of IrO_2, and were then calibrated through performing the FEFFIT of the EXAFS data of the IrO_2 reference sample, mainly to obtain the amplitude reduction factor (S_0^2) values. With S_0^2 known, the EXAFS data of the catalyst materials were fitted with such generated phase shifts and amplitudes. We also check with EXAFS spectra of back-to-OCV sample to have the full six coordinated Ir-O bonding. All those EXAFS fitting are done with K-range from 3 to 12$Å^{-1}$. For Co model-based EXAFS analysis, the same procedure was applied by using CoO as reference instead of IrO_2.

AUTHOR INFORMATION

Corresponding Author

xtzu@uestc.edu.cn, gum@sustc.edu.cn, and zhenxing.feng@oregonstate.edu.

Author Contributions

All the authors taken part in writing manuscript. the Chao Cai and Shaobo Han put forward the primary idea and completed the catalytic experiments. Maoyu Wang conducted the *in-situ* XAS experiments. Xiaotao Zu, Zhenxing Feng, and Meng Gu guided this work.

SUPPORTING INFORMATION

Supporting Information is available online. The extra electrochemical results, XRD, TEM, and XPS data can be found in Supporting Information.

ACKNOWLEDGMENT

This work is supported by the National Natural Science Foundation of China (21802065&U1830204), Guangdong Provincial Key Laboratory of Energy Materials for Electric Power with project no. 2018B030322001, and Guangdong Innovative and Entrepreneurial Research Team Program (2016ZT06N500), Shenzhen Peacock Plan (KQTD2016022620054656), Shenzhen Clean Energy Research Institute (No. CERI-KY-2019-003). Z. F. thanks the startup funding from Oregon State University. The XAS measurements were done at beamline 9-BM of the Advanced Photon Source, which is a U.S. Department of Energy (DOE) Office of Science User Facility operated for the DOE Office of Science by Argonne National Laboratory under Contract No. DE-AC02-06CH11357. Chao Cai, Maoyu Wang, and Shaobo Han are contributed to this work equally.

REFERENCES

(1) Wang, A.; Li, J.; Zhang, T., Heterogeneous Single-Atom Catalysis. *Nat. Rev. Chem.* **2018,** 2 (6), 65-81.

(2) Han, S.; Cai, C.; Yang, F.; Zhu, Y.; Sun, Q.; Zhu, Y.; Li, H.; Wang, H.; Shao-Horn, Y.; Sun, A. X.; Gu, M., Interrogation of the Reaction Mechanism in a Na-O_2 Battery Using In-Situ Transmission Electron Microscopy. *ACS Nano* **2020,** 14 (3), 3669–3677.

(3) Qiao, B.; Wang, A.; Yang, X.; Allard, L. F.; Jiang, Z.; Cui, Y.; Liu, J.; Li, J.; Zhang, T., Single-Atom Catalysis of CO Oxidation Using Pt1/FeOx. *Nat. Chem.* **2011,** 3 (8), 634-641.

(4) Wang, Q.; Xia, G.-J.; Zhao, Z. L.; Zhu, Y.; Shi, X.; Huang, L.; Wang, Y.-G.; Gu, M., Atomic Origin of CO-Interaction effect of PtPb@ Pt Catalyst Revealed by In Situ Environmental

Transmission Electron Microscopy. *Nano Energy* **2020,** 76, 105099.

(5) Wang, Q.; Zhao, Z. L.; Dong, S.; He, D.; Lawrence, M. J.; Han, S.; Cai, C.; Xiang, S.; Rodriguez, P.; Xiang, B., Design of Active Nickel Single-Atom Decorated MoS2 as a pH-Universal Catalyst for Hydrogen Evolution Reaction. *Nano Energy* **2018,** 53, 458-467.

(6) Zhao, Z. L.; Wang, Q.; Huang, X.; Feng, Q.; Gu, S.; Zhang, Z.; Xu, H.; Lin, Z.; Gu, M.; Li, H., Boosting Oxygen Evolution Reaction Using Defect-rich Ultra-Thin Ruthenium Oxide Nanosheets in Acidic Media. *Energy Environ. Sci.* **2020,** Advance Article, DOI: 10.1039/D0EE01960G.

(7) Cai, C.; Han, S.; Wang, Q.; Gu, M., Direct Observation of Yolk–Shell Transforming to Gold Single Atoms and Clusters with Superior Oxygen Evolution Reaction Efficiency. *ACS Nano* **2019,** 13 (8), 8865-8871.

(8) Cai, C.; Han, S.; Caiyang, W.; Zhong, R.; Tang, Y.; Lawrence, M. J.; Wang, Q.; Huang, L.; Liang, Y.; Gu, M., Tracing the Origin of Visible Light Enhanced Oxygen Evolution Reaction. *Adv. Mater. Interfaces* **2018**, 1801543.

(9) Han, S.; Cai, C.; Caiyang, W.; Xiang, X.; Deng, H.; Zu, X.; Lawrence, M. J.; Sun, K.; Gu, M., Interface Engineering to Enhance the Oxygen Evolution Reaction under Light Irradiation. *Appl. Phys. Lett.* **2019,** 115 (10), 103901.

(10) Cai, C.; Han, S.; Tang, Y., Engineering Oxygen Vacancies on Dendrite-Like IrO2 for the Oxygen Evolution Reaction in Acidic Solution. *Sustain. Energy Fuels* **2020,** 4 (5), 2462-2468.

(11) Wang, Q.; Huang, X.; Zhao, Z. L.; Wang, M.; Xiang, B.; Li, J.; Feng, Z.; Xu, H.; Gu, M., Ultrahigh-Loading of Ir Single Atoms on NiO Matrix to Dramatically Enhance Oxygen Evolution Reaction. *J. Am. Chem. Soc.* **2020,** 142 (16), 7425-7433.

(12) Wu, L.; Mendoza-Garcia, A.; Li, Q.; Sun, S., Organic Phase Syntheses of Magnetic Nanoparticles and Their Applications. *Chem. Rev.* **2016,** 116 (18), 10473-10512.

(13) Zhang, J.; Liu, J.; Xi, L.; Yu, Y.; Chen, N.; Sun, S.; Wang, W.; Lange, K. M.; Zhang, B., Single-Atom Au/NiFe Layered Double Hydroxide Electrocatalyst: Probing the Origin of Activity for Oxygen Evolution Reaction. *J. Am. Chem. Soc.* **2018,** 140 (11), 3876-3879.

(14) Cai, C.; Han, S.; Liu, W.; Sun, K.; Qiao, L.; Li, S.; Zu, X., Tuning Catalytic Performance by Controlling Reconstruction Process in Operando Condition. *Appl. Catal. B-Environ* **2020,** 260，118103.

(15) Wang, Q.; Zhao, Z. L.; Gu, M., CO Gas Induced Phase Separation in PtPb@ Pt Catalyst and Formation of Ultrathin Pb Nanosheets Probed by In Situ Transmission Electron Microscopy. *Small* **2019,** 15 (42), 1903122.

(16) Wang, Q.; Zhao, Z. L.; Zhang, Z.; Feng, T.; Zhong, R.; Xu, H.; Pantelides, S. T.; Gu, M., Sub-3 nm Intermetallic Ordered Pt3In Clusters for Oxygen Reduction Reaction. *Adv. Sci.* **2020,** 7 (2), 1901279.

(17) Nie, L.; Mei, D.; Xiong, H.; Peng, B.; Ren, Z.; Hernandez, X. I. P.; DeLariva, A.; Wang, M.; Engelhard, M. H.; Kovarik, L.; Datye, A. K.; Wang, Y., Activation of Surface Lattice Oxygen in Single-Atom Pt/Ce0(2) for Low-Temperature CO Oxidation. *Science* **2017,** 358 (6369), 1419-1423.

(18) Wang, Q.; Zhao, Z. L.; Dong, S.; He, D.; Lawrence, M. J.; Han, S.; Cai, C.; Xiang, S.; Rodriguez, P.; Xiang, B.; Wang, Z.; Liang, Y.; Gu, M., Design of active Nickel Single-Atom Decorated MoS2 as a pH-Universal Catalyst for Hydrogen Evolution Reaction. *Nano Energy* **2018,** 53, 458-467.

(19) Li, P.; Wang, M.; Duan, X.; Zheng, L.; Cheng, X.; Zhang, Y.; Kuang, Y.; Li, Y.; Ma, Q.; Feng, Z.; Liu, W.; Sun, X., Boosting Oxygen Evolution of Single-Atomic Ruthenium through Electronic Coupling with Cobalt-Iron Layered Double Hydroxides. *Nat. Commun.* **2019,** 10 (1), 1711.

(20) Alarawi, A.; Ramalingam, V.; He, J.-H., Recent Advances in Emerging Single Atom Confined

Two-Dimensional Materials for Water Splitting Applications. *Mater. Today Energy* **2019,** 11, 1-23.

(21) Hunt, S. T.; Milina, M.; Alba-Rubio, A. C.; Hendon, C. H.; Dumesic, J. A.; Roman-Leshkov, Y., Self-assembly of Noble Metal Monolayers on Transition Metal Carbide Nanoparticle Catalysts. *Science* **2016,** 352 (6288), 974-978.

(22) Yao, S.; Zhang, X.; Zhou, W.; Gao, R.; Xu, W.; Ye, Y.; Lin, L.; Wen, X.; Liu, P.; Chen, B.; Crumlin, E.; Guo, J.; Zuo, Z.; Li, W.; Xie, J.; Lu, L.; Kiely, C. J.; Gu, L.; Shi, C.; Rodriguez, J. A.; Ma, D., Atomic-Layered Au Clusters on Alpha-Moc As Catalysts for The Low-Temperature Water-Gas Shift Reaction. *Science* **2017,** 357 (6349), 389-393.

(23) Yang, H. B.; Hung, S.-F.; Liu, S.; Yuan, K.; Miao, S.; Zhang, L.; Huang, X.; Wang, H.-Y.; Cai, W.; Chen, R.; Gao, J.; Yang, X.; Chen, W.; Huang, Y.; Chen, H. M.; Li, C. M.; Zhang, T.; Liu, B., Atomically Dispersed Ni(I) as The Active Site for Electrochemical CO_2 Reduction. *Nat. Energy* **2018,** 3 (2), 140-147.

(24) Wei, S.; Li, A.; Liu, J.-C.; Li, Z.; Chen, W.; Gong, Y.; Zhang, Q.; Cheong, W.-C.; Wang, Y.; Zheng, L.; Xiao, H.; Chen, C.; Wang, D.; Peng, Q.; Gu, L.; Han, X.; Li, J.; Li, Y., Direct Observation of Noble Metal Nanoparticles Transforming to Thermally Stable Single Atoms. *Nat. Nanotech.* **2018,** 13 (9), 856-861.

(25) Zhang, Y.; Wu, C.; Jiang, H.; Lin, Y.; Liu, H.; He, Q.; Chen, S.; Duan, T.; Song, L., Atomic Iridium Incorporated in Cobalt Hydroxide for Efficient Oxygen Evolution Catalysis in Neutral Electrolyte. *Adv. Mater.* **2018,** 30 (18).

(26) Xu, L.; Jiang, Q.; Xiao, Z.; Li, X.; Huo, J.; Wang, S.; Dai, L., Plasma-Engraved Co3O4 Nanosheets with Oxygen Vacancies and High Surface Area for the Oxygen Evolution Reaction. *Angew. Chem. Int. Edit.* **2016,** 55 (17), 5277-5281.

(27) Babu, D. D.; Huang, Y.; Anandhababu, G.; Wang, X.; Si, R.; Wu, M.; Li, Q.; Wang, Y.; Yao,

J., Atomic Iridium@Cobalt Nanosheets for Dinuclear Tandem Water Oxidation. *J. Mater. Chem. A* **2019,** 7 (14), 8376-8383.

(28) Shen, J.; Li, Z.; Yan, Q.; Chen, Y., Reactions of Bivalent Metal Ions with Borohydride in Aqueous Solution for the Preparation of Ultrafine Amorphous Alloy Particles. *J. Phys. Chem.* **1993,** 97 (32), 8504-8511.

(29) Kalidindi, S. B.; Vernekar, A. A.; Jagirdar, B. R., Co-Co2B, Ni-Ni3B and Co-Ni-B Nanocomposites Catalyzed Ammonia-Borane Methanolysis for Hydrogen Generation. *Phys. Chem. Chem. Phys.* **2009,** 11 (5), 770-775.

(30) Sun, H.; Xu, X.; Yan, Z.; Chen, X.; Jiao, L.; Cheng, F.; Chen, J., Superhydrophilic Amorphous Co-B-P Nanosheet Electrocatalysts with Pt-like Activity and Durability for the Hydrogen Evolution Reaction. *J. Mater. Chem. A* **2018,** 6 (44), 22062-22069.

(31) Zhuang, L.; Ge, L.; Yang, Y.; Li, M.; Jia, Y.; Yao, X.; Zhu, Z., Ultrathin Iron-Cobalt Oxide Nanosheets with Abundant Oxygen Vacancies for the Oxygen Evolution Reaction. *Adv. Mater.* **2017,** 29 (17).

(32) Cai, C.; Mi, Y.; Han, S.; Wang, Q.; Liu, W.; Wu, X.; Zheng, Z.; Xia, X.; Qiao, L.; Zhou, W.; Zu, X., Engineering Ordered Dendrite-Like Nickel Selenide as Electrocatalyst. *Electrochim. Acta* **2019,** 295, 92-98.

(33) Yang, J.; Cai, C.; Li, Y.; Gao, L.; Guo, H.; Wang, B.; Pu, B.; Niu, X., In-situ Cobalt and Nitrogen Doped Mesoporous Graphitic Carbon Electrocatalyst via Directly Pyrolyzing Hyperbranched Cobalt Phthalocyanine for Hydrogen Evolution Reaction. *Electrochim. Acta* **2018,** 262, 48-56.

(34) Yang, J.; Guo, H.; Chen, S.; Li, Y.; Cai, C.; Gao, P.; Wang, L.; Zhang, Y.; Sun, R.; Niu, X.; Wang, Z., Anchoring and Space-Confinement Effects to Form Ultrafine Ru Nanoclusters for

Efficient Hydrogen Generation. *J. Mater. Chem. A* **2018,** 6 (28), 13859-13866.

(35) Wang, H.; Feng, E.-M.; Liu, Y.-M.; Zhang, C.-Y., High-Performance Hierarchical Ultrathin Sheet-Based Coooh Hollow Nanospheres with Rich Oxygen Vacancies for the Oxygen Evolution Reaction. *J. Mater. Chem. A* **2019**, 7 (13), 7777-7783.

(36) Wang, Q.; Zhao, Z.; Jia, Y.; Wang, M.; Qi, W.; Pang, Y.; Yi, J.; Zhang, Y.; Li, Z.; Zhang, Z., Unique Cu@ CuPt Core–Shell Concave Octahedron with Enhanced Methanol Oxidation Activity. *ACS Appl. Mater. Inter.* **2017,** 9 (42), 36817-36827.

(37) Han, S.; Zhu, Y.; Cai, C.; Zhu, J.; Han, W.; Chen, L.; Zu, X.; Yang, H.; Gu, M., Failure Mechanism of Au@Co9S8 Yolk-Shell Anode in Li-ion Batteries Unveiled by In-Situ Transmission Electron Microscopy. *Appl. Phys. Lett.* **2019,** 114 (11), 113901.

(38) Han, S.; Xia, G. J.; Cai, C.; Wang, Q.; Wang, Y. G.; Gu, M.; Li, J., Gas-Assisted Transformation of Gold from fcc to the Metastable 4H Phase. *Nat. Commun.* **2020,** 11 (1), 552.

(39) Stoerzinger, K. A.; Diaz-Morales, O.; Kolb, M.; Rao, R. R.; Frydendal, R.; Qiao, L.; Wang, X. R.; Halck, N. B.; Rossmeisl, J.; Hansen, H. A.; Vegge, T.; Stephens, I. E. L.; Koper, M. T. M.; Shao-Horn, Y., Orientation-Dependent Oxygen Evolution on RuO_2 without Lattice Exchange. *ACS Energy Lett.* **2017,** 2 (4), 876-881.

(40) Lee, Y.; Suntivich, J.; May, K. J.; Perry, E. E.; Shao-Horn, Y., Synthesis and Activities of Rutile IrO2 and RuO2 Nanoparticles for Oxygen Evolution in Acid and Alkaline Solutions. *J. Phys. Chem. Lett.* **2012,** 3 (3), 399-404.

(41) Li, P.; Wang, M.; Duan, X.; Zheng, L.; Cheng, X.; Zhang, Y.; Kuang, Y.; Li, Y.; Ma, Q.; Feng, Z.; Liu, W.; Sun, X., Boosting Oxygen Evolution of Single-Atomic Ruthenium through Electronic Coupling With Cobalt-Iron Layered Double Hydroxides. *Nat. Commun.* **2019,** 10.

(42) Wang, M.; Arnadottir, L.; Xu, Z. J.; Feng, Z., In Situ X-ray Absorption Spectroscopy Studies

of Nanoscale Electrocatalysts. *Nano-Micro Letters* **2019,** 11 (1), 47.

(43) Weng, Z.; Wu, Y.; Wang, M.; Jiang, J.; Yang, K.; Huo, S.; Wang, X.-F.; Ma, Q.; Brudvig, G. W.; Batista, V. S.; Liang, Y.; Feng, Z.; Wang, H., Active Sites of Copper-Complex Catalytic Materials for Electrochemical Carbon Dioxide Reduction. *Nat. Commun.* **2018,** 9.

(44) Minguzzi, A.; Lugaresi, O.; Achilli, E.; Locatelli, C.; Vertova, A.; Ghigna, P.; Rondinini, S., Observing the Oxidation State Turnover in Heterogeneous Iridium-Based Water Oxidation Catalysts. *Chem. Sci.* **2014,** 5 (9), 3591-3597.

(45) Ravel, B.; Newville, M., ATHENA, ARTEMIS, HEPHAESTUS: Data Analysis for X-ray Absorption Spectroscopy using IFEFFIT. *J. Synchrotron Radiat.* **2005,** 12, 537-541.